


Strong-field ionization of plasmonic nanoparticlesE. Saydanzad,¹ J. Li,^{1,2} and U. Thumm¹¹*Department of Physics, Kansas State University, Manhattan, Kansas 66506, USA*²*Department of Physics and Astronomy, Louisiana State University, Baton Rouge, Louisiana 70803, USA* (Received 18 November 2021; revised 2 July 2022; accepted 19 August 2022; published 6 September 2022)

We modeled strong-field ionization of metal nanoparticles by intense infrared laser pulses, accounting for and distinguishing in photoelectron (PE) momentum distributions the effects of PE correlation, PE–residual-charge interactions, PE rescattering and recombination, and transient laser-induced plasmonic fields. Our numerical results for 5-, 30-, and 70-nm-diameter gold nanospheres and peak laser-pulse intensities of 8.0×10^{12} and 1.2×10^{13} W/cm² show how PE velocity-map images are distinctly shaped by PE Coulomb repulsion, residual-charge accumulations, and plasmonic near fields. In contrast to gaseous atomic targets and dielectric nanoparticles, we find very large PE cutoff energies, for both directly emitted and rescattered PEs, that exceed the incident laser-pulse ponderomotive energy by two orders of magnitude.

DOI: [10.1103/PhysRevA.106.033103](https://doi.org/10.1103/PhysRevA.106.033103)**I. INTRODUCTION**

Exposed to intense laser light, atoms are excited or ionized. At sufficiently high light intensities, multiphoton or tunneling ionization occurs [1] and emitted photoelectrons (PEs) can gain a significant amount of energy while propagating in the oscillating laser electric field. For gaseous atomic targets, PEs that are directly emitted and do not return to the residual atom gain up to $2U_p(I_0)$ in kinetic energy in linearly polarized laser pulses, while PEs that are driven back to the residual ion by the laser electric field and rescatter elastically accumulate up to $10U_p(I_0)$ [2–5]. The ponderomotive energy $U_p(I_0) = I_0/4\omega^2$ is the cycle-averaged quiver energy of a free electron in a laser field of frequency ω and intensity I_0 .

Strong-field PE emission and rescattering from solids [6–12] and isolated nanostructures, such as clusters [13–17], nanotips [18–23], and isolated dielectric nanoparticles (NPs) [24–26], have been extensively studied throughout the past decade. Analogous to gaseous atoms, strong-field ionization leading to high PE energies from NPs can be thought of as occurring in distinct sequential steps [27]: electron emission from the NP surface, PE propagation in the continuum, and PE rescattering towards and interaction with the NP [17,26]. In comparison with gaseous atomic targets, each of these steps is significantly more intricate for clusters, nanotips, and NPs (both dielectric and metal), due to their more complex electronic and morphological structure and the emission of a much larger number of PEs, emphasizing the effects of PE correlation, residual charges, and PE–nanoplasmonic-field interactions (Fig. 1).

To simulate the PEs dynamics during the multiple ionization of dielectric NPs, a quasiclassical mean-field Monte Carlo model was developed employing classical Mie theory [28,29]. This model was applied to investigate PE angular distributions and laser-carrier-envelope-phase-controlled PE rescattering from 50- to 550-nm SiO₂ nanospheres [30], controlled near-field-enhanced electron acceleration from dielectric nanospheres [24], attosecond streaking spectroscopy

of electron scattering in dielectric nanoparticles [26], and ultrafast metallization of isolated dielectric and semiconducting NPs [31]. In this numerical model, electrons are liberated via tunnel ionization from randomly chosen surface atoms, based on Ammosov-Delone-Krainov atomic tunneling-ionization rates [32]. Photoelectrons are assumed to be launched at the classical tunnel exit with zero initial velocities. Their subsequent motion in the electric fields of the incident laser pulse and induced plasmonic response is propagated classically. Electronic correlation and PE–residual-charge interactions during the propagation are accounted for at the mean-field level. Cutoff energies for directly emitted and rescattered PEs from dielectric NPs were found to be $2\eta_{\text{pl}}^2 U_p(I_0)$ and $10\eta_{\text{pl}}^2 U_p(I_0)$, respectively [24]. In comparison to atomic targets, they are enhanced by the square of the plasmonic near-field enhancement factor η_{pl} . Experimentally, strong-field photoemission from isolated dielectric SiO₂ NPs by intense 25-fs 780-nm linearly polarized laser pulses was recently measured for different NP sizes and laser intensities by Powell *et al.* [33].

Metal NPs have been extensively investigated during the past two decades, owing to their remarkable optical properties [34,35]. These are largely related to incident light in the infrared (IR) to the visible frequency range enforcing the collective motion of conduction electrons. This light-driven excitation of localized surface-charge plasmons (LSPs) controls the NPs' light absorption, reflection, and skin depths [36]. It also results in a local (near the NP surface) nanoplasmonic field that can dramatically amplify the incident-laser electric field near the NPs plasmon resonance frequency [37,38]. The LSP resonance frequency can be tuned from IR to visible frequencies by synthesizing metal NPs' with specific shapes, sizes, compositions, and dielectric environments [35,39,40]. The tunable enhanced light absorption and scattering are key to powerful diagnostic methods, such as surface-enhanced Raman spectroscopy [41], femtosecond scanning tunneling microscopy and

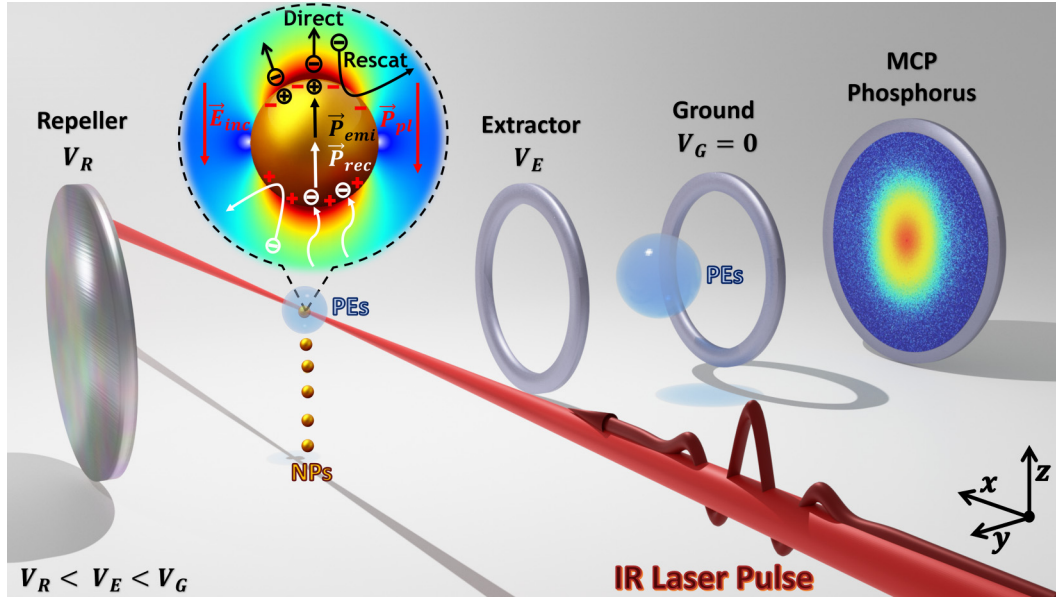


FIG. 1. Schematic of the velocity-map-imaging assembly. The incident IR laser pulse is linearly polarized in the z direction, propagates in the x direction, and intersects a beam of metal NPs. Here V_R , V_E , and V_G are the respective voltages on the PE repeller, extractor, and ground plates, needed to guide PEs to the multichannel-plate (MCP) phosphorus detector. The inset shows processes and fields that occur during the laser-NP interaction, including direct photoemission (Direct), PE rescattering (Rescat) and recombination, the incident laser electric field \vec{E}_{inc} , the induced plasmonic polarization \vec{P}_{pl} , and the emission (\vec{P}_{emi}) and recombination (\vec{P}_{rec}) dipoles with their corresponding charge distributions.

spectroscopy [19], time-resolved nanoplasmonic-field microscopy [38,42–44], biomedical and chemical sensing [45,46], and bioimaging, where plasmonic NPs are used as markers [47]. In addition, the controllable electro-optical properties of metal NPs enable promising applications, including the *in vivo* optoporation of targeted retinal ganglion cells with functionalized Au NPs [48], multichromatic switchable nanopixels [49], nanoplasmonically enhanced photocatalysis [50], plasmon-enhanced light harvesting [51,52], tumor detection and treatment [53,54], ultrafast electro-optical switching [55], and thermoplasmonics [56]. We recently proposed classical [57] and quantum-mechanical [58] schemes for the spatiotemporal imaging of induced plasmonic-field distributions near the surface of Au, Ag, and Cu NPs, based on nanometer spatially resolved attosecond PE streaking spectroscopy [57].

In the present work we extend the numerical modeling of atomic strong-field ionization to metal NPs (Fig. 1). We describe the release of the PE from the NP surface by intense short laser pulses based on Fowler-Nordheim tunneling rates [59] and subsequently sample over classical PE trajectories. We include and numerically evaluate for 5-, 30-, and 70-nm-diam gold nanospheres the effects of electronic repulsion, PE attraction by residual positive charges on the NP, multiple PE recollisions with the NP surface, PE recombination with the NP, and nanoplasmonic enhancement of the incident-laser-pulse electric field. We note that due to the strong plasmon response and a large number of free electrons, strong-field PE emission from metal NPs requires model assumptions different from strong-field emission from dielectric (insulator) targets. Our approach thus differs from the quasiclassical mean-field Monte Carlo model employing

classical Mie theory [30] with regard to the description of the NPs' plasmonic response and our implementation of adjusted Fowler-Nordheim tunneling rates [60]. Based on the simulated strong-field-driven PE current density and PE-emission- and recombination-induced dipole moments, we account for electronic excitations in the NP in terms of the electron temperature within a two-temperature model [61]. We allow for multiple electron-electron interactions while classically propagating a large number of PE trajectories rather than resorting to a mean-field description.

The paper is organized as follows. We continue with a description of our numerical model in Sec. II, in which we proceed by explaining our modeling of the nanoplasmonic field induced by the incident laser pulse (Sec. II A), the effect of emitted and recombined PEs on the NPs' evolving dipole moment (Sec. II B), the strong-field ionization and laser-driven current of released PEs (Sec. II C), and the Monte Carlo sampling of PE trajectories (Sec. II D). In Sec. III we discuss our numerical results for the strong-field ionization of gold nanospheres, distinguishing the influences of the transient laser-induced plasmonic field, residual charges, PE correlation, and PE rescattering and recombination in simulated velocity-map images (VMIs) (Sec. III A). Section III B covers different aspects of the photoemission dynamics, such as the accumulation of residual charges, the evolution of the number of propagated and recombined PEs, and the changing ratio of direct versus rescattered PE trajectories. In Secs. III C and III D we discuss the effects of NP size and laser intensity on PE momentum distributions (PEMDs) and cutoff energies. We summarize and present our conclusions in Sec. IV. Unless indicated otherwise, we use atomic units throughout this work.

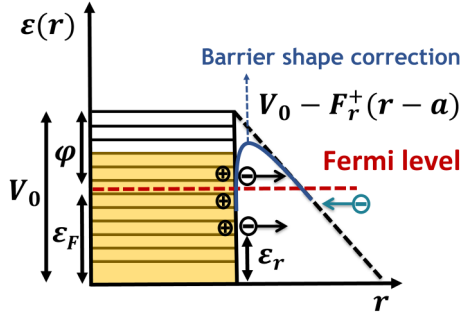


FIG. 2. Schematic of the conduction-band occupancy and effective strong-field-modified potential at the NP surface. Emitted and rescattered PEs are indicated by short black and turquoise horizontal arrows, respectively, together with the corresponding positive residual charges in the NP. The effective surface potential results from the superposition of an assumed rectangular surface-potential step and the potential of the total local electric-field radial component F_r^+ forms a triangular potential barrier on the negative side of the NP surface. This assumption is improved upon by the barrier-shape correction (blue solid line) (see Sec. II C 1).

II. THEORY

We investigate PE emission from metallic NPs by IR laser pulses with a Gaussian temporal profile. We assume the laser pulse propagates along the x axis and its electric field is linearly polarized along the z axis,

$$\vec{E}_{\text{inc}}(\vec{r}, t) = \sqrt{I_0} \exp\left(-2 \ln 2 \frac{(t - x/c)^2}{\tau^2}\right) \times \exp[-i\omega(t - x/c) + i\psi] \hat{e}_z, \quad (1)$$

where τ is the pulse length at full width at half-intensity maximum (FWHM), ω the pulse's central frequency, I_0 the peak laser intensity, ψ the carrier-envelope phase, and c the speed of light in vacuum (Fig. 1). In the assumed typical experimental setup, the laser pulse intersects a stream of isolated single NPs that are injected by aerodynamic lens focusing [26,30,62,63]. During the laser-NP interaction, LSPs are excited and induce an inhomogeneous plasmonic field near the NP surface. At the same time, and most significantly at the LSP resonance frequency [64,65], nonequilibrium high-energy electrons are excited in the metal NP due to strong light absorption, resulting in the population of excited electronic states above the Fermi level (Fig. 2). Sufficiently high laser intensities generate multiply ionized NPs [30,33]. As shown in the sketch of the experimental setup in Fig. 1, a fraction of the emitted PEs is guided to the detector and allows the recording of their projected momentum distributions as VMIs.

A. Induced plasmonic field

The incident laser pulse induces a transient dipole in the NP. In electric dipole approximation the corresponding plasmonic induced dipole moment $\vec{P}_{\text{pl}}(t) = (4\pi)^{-1} \alpha_{\text{Mie}}(\omega) \vec{E}_{\text{inc}}(\vec{r}, t)$ generates the induced plasmonic

electric field [66]

$$\vec{E}_{\text{pl}}(\vec{r}, t) = \frac{e^{ikr}}{r} \left[k^2 [\hat{e}_r \times \vec{P}_{\text{pl}}(t)] \times \hat{e}_r + \{3\hat{e}_r [\hat{e}_r \cdot \vec{P}_{\text{pl}}(t)] - \vec{P}_{\text{pl}}(t)\} \left(\frac{1}{r^2} - \frac{ik}{r} \right) \right], \quad (2)$$

where $k = 2\pi/\lambda = \omega/c$ is the central wave number of the incident pulse. Here $\alpha_{\text{Mie}}(\omega)$ is the complex NP polarizability. We calculate $\alpha_{\text{Mie}}(\omega)$ within Mie theory [28], following Ref. [67], which restricts the applicability of Eq. (2) to size parameters $S = ka \lesssim 0.6$ for nanospheres of radius a [43]. Since $\vec{E}_{\text{inc}}(\vec{r}, t)$ and $\vec{P}_{\text{pl}}(t)$ are aligned along the \hat{e}_z direction, Eq. (2) can be rewritten as

$$\vec{E}_{\text{pl}}(\vec{r}, t) = P_{\text{pl}}(t) \frac{e^{ikr}}{r^3} \{ [3(1 - ikr) - k^2 r^2] \sin\theta \cos\theta \hat{e}_\rho + [k^2 r^2 \sin^2\theta + (1 - ikr)(3 \cos^2\theta - 1)] \hat{e}_z \}, \quad (3)$$

where θ is the polar angle and \hat{e}_ρ and \hat{e}_z are the usual unit vectors in cylindrical coordinates.

For small size parameters S (strictly speaking, for $S \rightarrow 0$), the dependence of the complex NP polarizability $\alpha_{\text{Mie}}(\omega)$ on the dielectric function $\epsilon(\omega)$ given in [67,68] simplifies to the Clausius-Mossotti relation $\alpha_{\text{Mie}}(\omega) \approx 4\pi a^3 [\epsilon(\omega) - 1] / [\epsilon(\omega) + 2]$ [68]. Consequently, the vector sum of the incident and plasmonic electric fields on the NP surface reduces to

$$\vec{E}_{\text{inc}}(\vec{r}, t) + \vec{E}_{\text{pl}}(\vec{r}, t) \approx \frac{3E_{\text{inc}}(t)}{\epsilon(\omega) + 2} \{ [\epsilon(\omega) - 1] \cos\theta \hat{e}_r + \hat{e}_z \}. \quad (4)$$

Using $\epsilon(\omega) = -22.46 + i1.39$ for bulk gold at $\lambda = 780$ nm [69], the component of the electric field in the \hat{e}_z direction can be neglected. This results in the radial field

$$\vec{E}_{\text{inc}}(\vec{r}, t) + \vec{E}_{\text{pl}}(\vec{r}, t) \approx \frac{3P_{\text{pl}}(t) \cos\theta}{a^3} \hat{e}_r. \quad (5)$$

B. Generalized plasmon dipole moment

Since strong-field ionization of metal NPs by intense fields can lead to a large number of emitted and recombining PEs, the distribution of localized surface charges continuously varies while the NP is exposed to the plasmonically enhanced laser pulse intensity. This changes the effective dipole moment of the NP. We account for this change by modifying $\vec{P}_{\text{pl}}(t)$ for spherical NPs of radius a . During each laser half cycle the incident laser light augments the density of conduction electrons and holes on opposing hemispheres. The net effect of this periodic charge separation is quantified by the induced dipole moment $\vec{P}_{\text{pl}}(t)$ and the local charge density at any position $\vec{r}_s = (a, \theta, \phi)$ on the NP's surface,

$$\sigma_{\text{pl}} = \frac{1}{4\pi} [\vec{E}_{\text{inc}}(\vec{r}_s, t) + \vec{E}_{\text{pl}}(\vec{r}_s, t)] \cdot \hat{e}_r \quad (6)$$

$$\approx 3\epsilon_0 P_{\text{pl}}(t) \cos\theta / a^3, \quad (7)$$

where the approximate equation (7) follows from Eq. (5). Thus, σ_{pl} is approximately proportional to $\cos\theta$.

We assume surface-charge redistributions induced by the laser electric field and PEs to occur instantaneously. This assumption is supported by an estimate of the charge equilibration time based on the continuity equation $-\partial\rho/\partial t = \nabla \cdot (\kappa \vec{E}) \approx \kappa \nabla \cdot \vec{E}$, relating the charge density ρ to the electric field \vec{E} and conductivity κ [70]. Applying Gauss's law then leads to the differential equation $\partial\rho/\partial t = -\kappa\rho/(\epsilon_0\epsilon)$ with the solution $\rho(t) = \rho_0 \exp(-t/T_r)$. Inserting material constants for gold, $\kappa = 35.2 \times 10^6$ S/m [71], and the dielectric constant $\epsilon = 22.5$ [69] yields the relaxation time $T_r = \epsilon_0\epsilon/\kappa = 5.6$ as. This time is smaller than the time intervals $dt = T/48 = 54.2$ as, where $T = 2\pi/\omega$ is the laser optical cycle, after which we update in our numerical propagation of PE trajectories (cf. Sec. IID 1 below) electric fields, charge distributions, and numbers of emitted and recombined photoelectrons.

Based on the approximately dipolar electric-field response in Eq. (5), we expect a mostly dipolar distribution of emitted and recombining electrons. In addition to the directly laser-driven-induced plasmonic charge redistribution σ_{pl} , PE emission and rescattering (discussed in Secs. IIC 1 and IID 2 below) modify the NP surface-charge density, decreasing σ_{pl} by

$$\sigma_{\text{emi}} \approx -\frac{n_{\text{emi}}(t_{\text{cyc}}, t)}{\pi a^2} \cos \theta, \quad (8)$$

$$\sigma_{\text{rec}} \approx -\frac{n_{\text{rec}}(t_{\text{cyc}}, t)}{\pi a^2} \cos \theta, \quad (9)$$

respectively. The accumulated number of emitted PEs is

$$n_{\text{emi}}(t_{\text{cyc}}, t) = \left[\int_{t_{\text{cyc}}}^t dn_{\text{emi}} \right], \quad (10)$$

where the outer square brackets denote rounding to the nearest integer value. The incremental change in the number of emitted electrons $dn_{\text{emi}}(t)$ is given by Eq. (15) below. Here t_{cyc} denotes the initial time of the half cycle considered, starting at $\vec{E}_{\text{inc}}(t_{\text{cyc}}) = 0$. Similarly, $n_{\text{rec}}(t_{\text{cyc}}, t)$ is the number of recombined PEs on the positive side of the NP during the same time interval. We assume recombination on the negative side of the NP dipole to be ignorable, since our numerical applications indicate large negative residual charge distributions, leading to dominant rescattering from the NP (Secs. IID 2 and III below). We calculate $n_{\text{rec}}(t_{\text{cyc}}, t)$ in each half cycle numerically by tracking all PE trajectories.

The negative space charge provided by outgoing PEs on the negative side and incoming PEs on the positive side of the NP surface triggers a collective electronic response that modifies the NP's surface-charge density. This plasmonic response can be thought of as the buildup of image charges during each laser half cycle. The net image charge may be large if PEs are emitted or are approaching the NP surface in spatial and temporal proximity. One might thus ask to what extent this affects the surface-charge density. To estimate the image-charge effect on the surface-charge density, we calculate the image-charge surface densities induced by PE emission and recombination during each laser half cycle by adding contributions from small time intervals $[t - 2dt, t]$

and $[t - dt, t + dt]$,

$$\Delta\sigma_{\text{emi}}^{\text{img}} \approx -\frac{n_{\text{emi}}(t - 2dt, t)}{\pi a^2} \cos \theta, \quad (11)$$

$$\Delta\sigma_{\text{rec}}^{\text{img}} \approx \frac{n_{\text{rec}}(t - dt, t + dt)}{\pi a^2} \cos \theta, \quad (12)$$

respectively. Our numerical tests show that these changes of the surface-charge density can be neglected in comparison to σ_{emi} and σ_{rec} .

The electron density decreases on the negative side and the hole density on the positive side of the NP dipole due to intracycle PE emission and recombination, respectively. Integration over the corresponding hemispheres of the NP surface results in the time-dependent polarizations

$$\begin{aligned} \vec{P}_{\text{emi}}(t) &= \int ds \vec{r}_s \sigma_{\text{emi}}, \\ \vec{P}_{\text{rec}}(t) &= \int ds \vec{r}_s \sigma_{\text{rec}}. \end{aligned} \quad (13)$$

These are antiparallel to $\vec{P}_{\text{pl}}(t)$ and thus reduce the plasmonic field $\vec{E}_{\text{pl}}(\vec{r}, t)$, as illustrated in the inset in Fig. 1. Taking the effects of intracycle PE emission and recombination on the induced NP polarization into account, we introduce the generalized induced dipole polarization

$$\begin{aligned} \vec{P}_G(t) &= \vec{P}_{\text{pl}}(t) + \vec{P}_{\text{emi}}(t) + \vec{P}_{\text{rec}}(t) \\ &= \vec{P}_{\text{pl}}(t) - \frac{2}{3}a[n_{\text{emi}}(t_{\text{cyc}}, t) + n_{\text{rec}}(t_{\text{cyc}}, t)] \frac{\vec{E}_{\text{inc}}(t)}{E_{\text{inc}}(t)} \end{aligned} \quad (14)$$

and replace $\vec{P}_{\text{pl}}(t)$ in Eq. (2) by $\vec{P}_G(t)$ in our calculations. Equation (14) shows that intracycle PE emission and recombination reduce the plasmonic field strength, especially for larger NPs. Therefore, any physical process that increases the number of emitted or recombined PEs tends to weaken the effective nanoplasmonic field related to the (generalized) dipole moment $\vec{P}_G(t)$, depending on the characteristics of both the incident laser-pulse properties (wavelength, peak intensity, pulse amplitude, and polarization profile) and NP properties (composition, shape, and size). For example, for incident laser-pulse frequencies close to the LSP resonance, we expect the nanoplasmonic field enhancement to increase n_{emi} and n_{rec} and to noticeably decrease $\vec{P}_G(t)$.

C. Strong-field ionization

We describe strong-field ionization from metal NPs within a semiclassical approach including (1) PE emission based on quantum-mechanical tunneling, (2) PE propagation to the detector by sampling over classical trajectories, and (3) PE rescattering and recombination at the NP surface.

1. Photoelectron emission

The number of PEs emitted at time t during a small time interval dt ,

$$dn_{\text{emi}}(t) = \left[dt \int_0^{2\pi} d\phi \int_0^\pi d\theta a^2 \sin \theta J_r(\vec{r}_s, t) \right], \quad (15)$$

is given by the radial PE current density at time t at the position $\vec{r}_s = (a, \theta, \phi)$ [59],

$$\begin{aligned} J_r(\vec{r}_s, t) &= \int_{-\infty}^{\infty} d\vec{p} g(\vec{p}) f_{\text{FD}}(\vec{p}) W(p_r, F_r^+) p_r \\ &= \frac{k_B T_e}{2\pi^2} \int_0^{V_0} d\varepsilon_r W(\varepsilon_r, F_r^+) \ln \left[1 + \exp \left(\frac{\varepsilon_F - \varepsilon_r}{k_B T_e} \right) \right], \end{aligned} \quad (16)$$

in terms of the number of states per unit momentum volume within the Sommerfeld theory of metals $g(\vec{p}) = (4\pi^3)^{-1}$ [71], the Fermi-Dirac distribution function $f_{\text{FD}}(\vec{p}) = \{\exp[(\varepsilon - \varepsilon_F)/k_B T_e] + 1\}^{-1}$, and the tunneling ionization rate $W(\varepsilon_r, F_r^+)$. Here $\varepsilon = \varepsilon_r + \varepsilon_{\text{tan}}$ is the conduction-electron energy, ε_F the Fermi energy, k_B the Boltzmann constant, and T_e the absolute electron temperature. In addition, $\varepsilon_r = p_r^2/2$ and ε_{tan} are the electron kinetic energies in the radial and tangential directions with respect to the NP surface, respectively. Further, $F_r^+ = |\vec{F}(\vec{r}_s, t) \cdot \hat{e}_r|$ designates the magnitude of the radial component of the total electric field at the NP surface,

$$\vec{F}(\vec{r}_s, t) = \vec{E}_{\text{inc}}(\vec{r}_s, t) + \vec{E}_{\text{pl}}(\vec{r}_s, t) + \vec{F}_{\text{res}}(\vec{r}_s, t). \quad (17)$$

The number of residual charges at time t is equal to the number of propagated PEs, which is the difference of all emitted PEs $n_{\text{emi}}(t_0, t)$ [calculated from Eq. (15)] and all recombined PEs $n_{\text{rec}}(t_0, t)$ (calculated numerically by tracking all trajectories). The initial time t_0 is chosen before the onset of the laser pulse. In addition to the external-field-induced dipolar surface-charge redistributions discussed in Sec. II B above, the accumulation of residual charges generates a monopole contribution to the net induced electric field at any point $\vec{r}_s = (a, \theta, \phi)$ on the NP surface,

$$\vec{F}_{\text{res}}(\vec{r}_s, t) = \frac{[n_{\text{emi}}(t_0, t) - n_{\text{rec}}(t_0, t)] \vec{r}_s}{|\vec{r}_s|^3}. \quad (18)$$

Based on Eqs. (10) and (13), we self-consistently calculate $\vec{F}_{\text{res}}(\vec{r}_s, t)$ and $\vec{F}(\vec{r}_s, t)$.

We model tunneling ionization by adapting the PE-emission rate first derived for static electric fields and a triangular potential barrier by Fowler and Nordheim [59] and later modified by Murphy and Good [72],

$$\begin{aligned} W(\varepsilon_r, F_r^+) &\cong 4 \frac{\sqrt{\varepsilon_r(V_0 - \varepsilon_r)}}{V_0} \\ &\times \exp \left(-\frac{4\sqrt{2}}{3F_r^+} \nu(f)(V_0 - \varepsilon_r)^{3/2} \right), \end{aligned} \quad (19)$$

allowing for a parametric dependence on time of the outward-pointing radial field component F_r^+ . Here φ is the work function and $V_0 = \varepsilon_F + \varphi$ the electronic potential at the bottom of the conduction band relative to the continuum threshold. The numerically calculated barrier-shape-correction factor $\nu(f)$ accounts for the lowering of the surface-potential barrier due to the attractive PE self-image interaction and significantly increases the PE emission rate [72]. An analytical approximation, valid for sufficiently small scaled electric-field strengths $f = F_r^+/(V_0 - \varepsilon_r)^2$, was derived by Forbes [73] as $\nu(f) \approx 1 - f + \frac{1}{6}f \ln(f)$. This approximation is exact for $f = 0, 1$ and has an absolute error below 0.0025 for $0 < f < 1$ [60]. For the numerical applications presented in this study $0 <$

$f < 1.15$. Strong electric fields at the NP surface and high electron temperatures can excite electrons above the potential barrier. In these cases f is larger than one and we assume electron emission by over-the-barrier transitions to occur by setting the ionization probability equal to one.

2. Electron temperature

Before being exposed to the laser pulse, the electron temperature T_e and lattice temperature T_l of the NP are in equilibrium and typically between 100 and 300 K. The effects of these initial temperatures on PE emission from metal NPs are ignorable within the accuracy of current strong-field experiments, due to strong electronic heating by the laser pulse and short laser-pulse duration on the timescale of lattice heating. To account for electronic heating by the incident laser pulse, we calculate T_e in Eq. (16) by adapting the two-temperature model originally proposed by Anisimov *et al.* [61]. According to this model, T_e , T_l , and the energy $Q \simeq \sigma_{\text{abs}} I_{\text{inc}}(t)/V$ absorbed per unit time and volume by a NP of volume $V = \frac{4}{3}\pi a^3$ [74] are related by the coupled diffusion equations [75]

$$\begin{aligned} C_e \frac{\partial T_e}{\partial t} &= \vec{\nabla} \cdot (K_e \vec{\nabla} T_e) - G(T_e - T_l) + Q, \\ C_l \frac{\partial T_l}{\partial t} &= \vec{\nabla} \cdot (K_l \vec{\nabla} T_l) + G(T_e - T_l). \end{aligned} \quad (20)$$

Here $\sigma_{\text{abs}} = k \text{Im}[\alpha_{\text{Mic}}(\omega)]$ is the absorption cross sections [76] and $I_{\text{inc}}(t)$ the instantaneous incident laser intensity. In addition, $C_e = \gamma T_e$, C_l , K_e , K_l , and G are the heat capacities of the electrons and lattice, the thermal conductivities of the electrons and lattice, and the electron-phonon coupling constant, respectively. We refer to the electronic heat capacity of an ideal Fermi gas that increases linearly in T_e with proportionality factor γ (heat-capacity constant) [71].

For laser-pulse lengths τ much shorter than typical electron-gas equilibration times (which are of the order of picoseconds [77]), we may neglect electron-lattice couplings. For ultrashort laser pulses, energy transfer from the electron gas to the NP lattice is thus irrelevant during the laser-NP interaction and T_e strongly increases due to laser heating, while the lattice temperature remains constant. In addition, with regard to the small NP size, we assume the electron thermal conduction term $\vec{\nabla} \cdot (K_e \vec{\nabla} T_e)$ can be neglected in Eqs. (20) such that T_e is spatially homogeneous. Under these assumptions Eqs. (20) simplify to

$$\begin{aligned} \gamma T_e \frac{dT_e}{dt} &= \frac{\sigma_{\text{abs}} I_{\text{inc}}(t)}{\frac{4}{3}\pi a^3}, \\ T_e(t_0) &= T_l \end{aligned} \quad (21)$$

and can be solved numerically to yield $T_e(t)$. Knowing $T_e(t)$, we solve Eqs. (14)–(16) numerically to find the number of emitted PEs and generalized induced dipole moment $P_G(t)$ at any time.

D. Sampling over photoelectron trajectories

Based on the radial current density of electrons released at the NP surface by tunneling ionization (16), we sample over classical PE trajectories, including the effects of PE repulsion,

PE–residual-charge interactions, and PE correlation, rescattering, and recombination.

1. Photoelectron trajectories

Starting at initial phase-space points $\{(\vec{r}_{i,0}, \vec{v}_{i,0})\}$, we propagate Newton's equations of motion for $n_{\text{pro}}(t) = n_{\text{emi}}(t_0, t) - n_{\text{rec}}(t_0, t)$ PEs. We thus track the correlated PE motion outside the NP (for $r \geq a$) by numerically solving $6n_{\text{pro}}(t)$ coupled ordinary differential equations

$$\begin{aligned} \frac{d\vec{v}_i}{dt} &= -\vec{F}(\vec{r}_i, t) + \vec{F}_{e-e}(\vec{r}_i, \vec{r}_j) + \vec{F}_{\text{img}}(\vec{r}_i), \\ \frac{d\vec{r}_i}{dt} &= \vec{v}_i, \end{aligned} \quad (22)$$

where $i = 1, \dots, n_{\text{pro}}(t)$. Coulomb interactions between PEs are given by the electric fields

$$\vec{F}_{e-e}(\vec{r}_i, \vec{r}_j) = \frac{1}{2} \sum_{j \neq i}^{n_{\text{pro}}(t)} \frac{\vec{r}_i - \vec{r}_j}{|\vec{r}_i - \vec{r}_j|^3} \quad (23)$$

and PE–image-charge interactions for a charged-insulated conduction sphere by [66]

$$\vec{F}_{\text{img}}(\vec{r}_i) = -\frac{\vec{r}_i a^3}{r_i r_i^3} \frac{2r_i^2 - a^2}{(r_i^2 - a^2)^2}. \quad (24)$$

Our numerical tests revealed no visible influence of image-charge–PE interactions on (observable) PE momentum distributions. We attribute this insensitivity to emitted and recombining PEs spending a very short time near the NP surface, while $\vec{F}_{\text{img}}(\vec{r}_i)$ is relatively strong, such that, on average, image-charge interactions are weak in comparison to other PE interactions.

We numerically integrate the classical equations of motion (22) by using a fourth-order Runge-Kutta algorithm, starting PE trajectories at times $t_{i,0}$ with zero initial velocities at positions $\vec{r}_{i,0}$. We update $n_{\text{pro}}(t)$ in each time interval $dt = T/48 = 54.2$ as. For this value of dt we obtain converged PE momentum distributions. The start positions are chosen at the tunnel exit for tunneling ionization and at the NP surface for over-the-barrier ionization. We terminate the classical propagation either when a PE recombines at the NP surface or when the PE velocity becomes constant within a very small preset tolerance interval. Typical propagation times in our numerical applications are of the order of 1 ps.

2. Photoelectron rescattering and recombination

During the laser-NP interaction, emitted PEs can be driven back to collide with the NP by the laser pulse. Depending on the direction of the total electric field $\vec{F}(\vec{r}_s, t)$ at the surface, we distinguish two cases. (i) We assume that PEs that are driven by $\vec{F}(\vec{r}_s, t)$ to the NP surface on the positive hemisphere of the induced dipolar NP charge distribution either rescatter, if their energies ε (relative to the valence-band bottom) exceed the surface-potential step V_0 , or recombine into bound conduction band states, if $\varepsilon < V_0$. (ii) In contrast, we assume that PEs that are driven to the NP surface on the negative hemisphere always rescatter.

In our numerical applications in Sec. III we distinguish and compare specular and diffusive PE rescattering at the NP

surface. In both cases we conserve the PE kinetic energy. For diffusive rescattering we uniformly randomize the polar and azimuthal scattering angles relative to the surface normal at the impact site \vec{r}_s on the NP surface, thereby modeling rescattering in all accessible directions with equal probability. Our numerical results predict that a considerable number of PEs cannot escape against the attractive Coulomb force of the residual charges. These PEs may undergo several rescattering cycles and are assumed to recombine with the NP (cf. Sec. III B).

3. Monte Carlo sampling

We include PE trajectories by Monte Carlo sampling over their initial phase-space points $\{(\vec{r}_{i,0}, \vec{v}_{i,0})\}$ in each time interval $[t, t + dt]$. This sampling is carried out based on the separable model probability-density function (PDF) $\rho(\vec{r}_{i,0}, \vec{v}_{i,0}, t) = \rho_{\text{pos}}(\vec{r}_{i,0}, t) \rho_{\text{vel}}(\vec{v}_{i,0}, t)$ that lends relative weights to the trajectories. Assuming zero initial velocities $\vec{v}_{i,0}$ for all PEs at the tunnel exit and in spherical coordinates, the phase-space PDF reduces to the velocity-independent function $\rho_{\text{pos}}(\vec{r}_{i,0}, t) = \rho_{\text{pos}}(a, \phi_{i,0}, \theta_{i,0}, t)$. We introduce $\rho_{\text{pos}}(a, \phi_{i,0}, \theta_{i,0}, t)$ phenomenologically as being proportional to the radial probability current density $J_r(\vec{r}_s, t)$ at the NP surface (16),

$$\rho_{\text{pos}}(a, \phi_{i,0}, \theta_{i,0}, t) \propto J_r(a, \phi_{i,0}, \theta_{i,0}, t). \quad (25)$$

Based on Eqs. (16) and (19), Fowler and Nordheim [59] and Forbes [78] evaluated the radial probability current density for PE emission near the Fermi level at room temperature as

$$J_r \propto F_r^{+2} \exp\left(-\frac{4\sqrt{2}}{3F_r^+} \nu(f) \varphi^{3/2}\right). \quad (26)$$

In the weak-field limit (small F_r^+), PE emission is negligible. Conversely, large radial field components F_r^+ are approximately proportional to the plasmonically enhanced laser electric field $|\vec{E}_{\text{inc}}(a, \phi_{i,0}, \theta_{i,0}, t) + \vec{E}_{\text{pl}}(a, \phi_{i,0}, \theta_{i,0}, t) \cdot \hat{e}_r|$ on the NP surface.

For a conducting sphere, tunneling ionization is solely driven by the radial component of the electric field at the surface, $[\vec{E}_{\text{inc}}(a, \phi_{i,0}, \theta_{i,0}, t) + \vec{E}_{\text{pl}}(a, \phi_{i,0}, \theta_{i,0}, t)] \cdot \hat{e}_r$, which is approximately proportional to $\cos \theta_{i,0}$ for small size parameters S (cf. Sec. II A). We are thus led to sample over the initial polar angle of the PE with the PDF

$$\rho_{\text{pos}}(\vec{r}_{i,0}) \approx \frac{4}{\pi} \cos^2 \theta_{i,0} \quad (27)$$

over the interval $[0, \pi/2]$ or $[\pi/2, \pi]$, depending on the direction of the electric field in the relevant laser half cycle, and pick the azimuthal PE start angle $\phi_{i,0}$ randomly and uniformly in the interval $[0, 2\pi]$ [79]. Our numerical calculations show that the probability of having two electron-trajectory-start positions coincide is extremely small and statistically irrelevant. In order to avoid the rare and physically irrelevant occurrence of numerical instabilities due to the Coulomb singularity of the repulsive PE interaction, we impose a lower limit on the separation of PE-trajectory-start positions. In each time interval $dt = T/48 = 54.2$ as, we opt for PEs to start their motion from the NP surface with an initial separation of at least 4.86 a.u. This distance corresponds to the free-electron density of gold, 8.7×10^{-3} a.u.⁻³ [71].

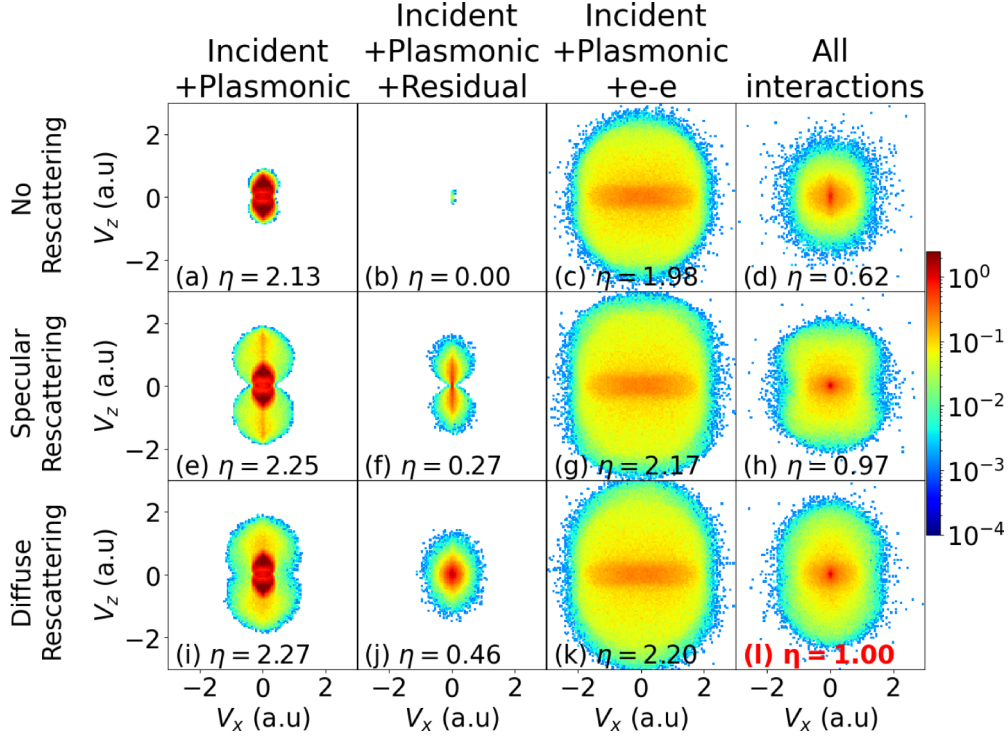


FIG. 3. Photoelectron VMIs simulated for 30-nm-diameter gold nanospheres (a)–(d) excluding PE rescattering and including either (e)–(h) specular or (i)–(l) diffuse PE rescattering for incident 780-nm laser pulses with a pulse length of 25 fs (FWHM) and 8.0×10^{12} W/cm² peak intensity. Columns 1–3 show simulations where only selected PE interactions are included. In column 1 only the incident laser and plasmon fields (\vec{E}_{inc} and \vec{E}_{pl}) are included. Column 2 adds PE interactions with residual positive charges (\vec{F}_{res}). The VMIs in column 3 include \vec{E}_{inc} , \vec{E}_{pl} , and repulsive PE Coulomb interactions (\vec{F}_{e-e}). Simulations including all PE interaction are shown in column 4. The parameter η gives integrated PE yields normalized to the integrated yield from the VMI in graph (l): (a) $\eta = 2.13$, (b) $\eta = 0.00$, (c) $\eta = 1.98$, (d) $\eta = 0.62$, (e) $\eta = 2.25$, (f) $\eta = 0.27$, (g) $\eta = 2.17$, (h) $\eta = 0.97$, (i) $\eta = 2.27$, (j) $\eta = 0.46$, (k) $\eta = 2.20$, and (l) $\eta = 1.00$.

In a typical experimental setup, gaseous targets are exposed to a spatially varying laser intensity. To account for the spatial intensity profile of the laser pulse, we focal-volume average over the laser beam, randomly choosing r' and z' from the Gaussian intensity profile,

$$I_0(r', z') = I_0 \left(\frac{w_0}{w(z')} \right)^2 \exp \left(\frac{-2r'^2}{w(z')^2} \right), \quad (28)$$

where r' is the radial distance from the central symmetry axis of the laser beam, z' is the axial distance from the beam's focus, w_0 is the waist radius, and $w(z') = w_0 \sqrt{1 + (z'/z_R)^2}$, with the Rayleigh range $z_R = \pi w_0^2 / \lambda$. In our numerical applications for a given nominal peak intensity I_0 , we find converged PEMDs by adding the PE yields from up to 5000 randomly sampled peak laser intensities $I_0(r', z')$. The number of intensities required for convergence depends on the NP size and is larger for smaller NPs.

III. NUMERICAL RESULTS: PHOTOELECTRON MOMENTUM DISTRIBUTIONS

A. Influence of the nanoplasmonic field, rescattering, PE-residual-charge interactions, and PE correlation

Photoelectron momentum distributions are sensitive to all PE interactions included in our simulation with regard to both strong-field-induced electron emission at the NP surface by tunneling and subsequent PE propagation. The tunneling

release of PEs strongly depends on the radial component of the total electric field \vec{F} (17). Stronger incident and plasmonic fields increase the number of propagating PEs and PE yield, while PE recombination and the accumulation of positive residual charges on the NP decrease the yield. Photoelectron self-image-charge interactions increase the PE-emission rate by lowering the potential barrier (cf. Sec. II C 1). In order to track the effects of different electronic interactions on the propagation and rescattering of released PEs, we leave the modeling of the tunneling release of electrons at the NP surface unchanged (for identical laser-pulse parameters), assuming for all calculated VMIs identical tunnel-ionization rates (19). The comparison of simulations in which we selectively include and exclude specific PE interactions during the PE propagation and rescattering only allows us to quantify their specific effects on PEMDs.

Figure 3 shows simulated PE VMIs for gold nanospheres 30 nm in diameter for the experimental setup depicted in Fig. 1. The VMIs are projections of the PEMD on the x - z plane of the MCP detector and show the projected PE yields as functions of the PE asymptotic velocities v_x and v_z along the laser propagation and laser polarization directions. The incident Gaussian laser pulses have a pulse length of $\tau = 25$ fs FWHM (ten cycles), central angular frequency $\omega = 2.415$ PHz (corresponding to the wavelength $\lambda = 780$ nm), and peak intensity of $I_0 = 8.0 \times 10^{12}$ W/cm². We represent the electronic structure of the NPs in terms of the

surface-potential step $V_0 = \varepsilon_F + \varphi$ with the work function $\varphi = 5.1$ eV and Fermi energy $\varepsilon_F = 8.0$ eV for bulk gold [80], initial electron and lattice temperatures $T_e(t_0) = 300$ K, and heat-capacity constant $\gamma = 66$ J/(m³ K²) [71].

Figures 3(a)–3(d), 3(e)–3(h), and 3(i)–3(l) include simulation results obtained under the assumption of no PE reflection at the NP surface, specular reflection, and diffuse reflection, respectively, as described in Sec. IID 2. For the simulations without rescattering, PEs that are driven back to the NP surface are assumed to recombine. The first column in this figure shows simulated VMIs for which the effects of the electric fields of residual charges (\vec{F}_{res}) and PE-PE Coulomb interactions (\vec{F}_{e-e}) are neglected during the PE propagation. In the second column \vec{F}_{e-e} is switched off, while \vec{F}_{res} is disregarded in the third column. In column 4 all PE interactions are included. To allow for a qualitative and quantitative comparison, we normalized the yields in all graphs to the largest yield in Fig. 3(l) and display the normalized integrated yield factor η in each graph. We calculate this factor as the v_x - and v_z -integrated yields from the VMIs in Figs. 3(a)–3(k) divided by the integrated yield of Fig. 3(l). We choose Fig. 3(l) as a reference since it displays our most realistic and accurate simulation results. The comparison of the VMIs in Fig. 3 allows us to assess the influence of the following PE interactions on VMIs.

1. Rescattering

The VMIs in Figs. 3(a)–3(d), calculated without allowing for PE rescattering, overemphasize PE recombination. The corresponding enhanced accumulation of positive residual charges on the NP decreases the PE yield. Indeed, the PE yields in Figs. 3(a)–3(d) are consistently smaller than for simulations that allow for PE rescattering [Figs. 3(e)–3(h) and 3(i)–3(l)]. The reduction of the PE yield is most pronounced in the second column and easily recognized by much smaller relative yields η in Fig. 3(b). It remains relevant for simulations that include all PE interactions, shown in column 4, where the suppression of rescattering and ensuing enhanced recombination reduces the relative yield to 62% in Figs. 3(a)–3(d). While still clearly noticeable, this reduction in PE yield upon disabling rescattering is less visible in simulations that exclude residual-charge interactions in column 3. In this case, PE rescattering still occurs for the simulation in Figs. 3(e)–3(h) and 3(i)–3(l), but is much less likely, due to the absence of attractive PE–residual-charge interactions. At the same time, the added PE Coulomb repulsion strongly inflates the yields in all panels of column 3.

2. Plasmonic-field interactions

The simulated VMIs in first column of Fig. 3 are calculated under the assumption that released electrons solely interact with the incident laser and induced plasmonic field while propagating to the detector. These PE distributions are aligned with the laser-polarization direction and have a dipolelike appearance, owing to the dipole character transferred from the induced plasmonic field and tunneling ionization.

Since Fig. 3(a) excludes rescattering, its comparison with Figs. 3(e) and 3(i) reveals that directly emitted PEs dominate the low-energy part of the photoemission spectra. Rescattered

electrons, in contrast, can gain additional energy from the laser and induced plasmonic fields and establish the higher-energy part of the PE spectrum. Rescattering boosting PE energies is a well-understood phenomenon in strong-field ionization. For gaseous atomic targets, elastically rescattered PEs reach kinetic energies up to $10U_p(I_0)$ [2–5] and significantly larger energies for dielectric NPs (SiO₂) [24,30,33]. By comparing the yield factors η in the first column, we find that approximately 94% of the detected PEs are directly emitted, while 6% have rescattered at the NP surface at least once.

3. Residual-charge interactions

The second column of Fig. 3 displays the effects of PE residual-charge interactions on VMIs. These simulation results are obtained by solving Newton’s equations (22) for the propagation of released electrons under the influence of the electric fields of the incident laser \vec{E}_{inc} (1), induced plasmonic dipole \vec{E}_{pl} (3), and residual charges \vec{F}_{res} (18). Photoelectron correlation \vec{F}_{e-e} (23) is neglected.

The long-range Coulomb attraction of accumulating positive residual charges decelerates both direct and rescattered PEs. It increases the number of PEs that recombine with or rescatter off the NP. Therefore, residual charge interactions tend to decrease the net PE yield and cutoff energy. This is clearly demonstrated by comparing the VMIs and relative PE yields η in the second column with the results shown in the first column. This comparison also reveals that the strong PE–residual-charge attraction practically eliminates direct PE emission [Fig. 3(b)]. Without being rescattered, emitted PEs cannot accumulate enough energy in the laser and plasmonic fields to overcome the residual-charge attraction.

Allowing for specular PE reflection in Fig. 3(f) and diffuse rescattering in Fig. 3(j), some of the rescattered PEs gain enough energy from the laser pulse to beat the residual-charge attraction and escape to the PE detector. While \vec{F}_{res} preserves the dipolar PE distribution for specular rescattering in Fig. 3(f), the dipolelike character of the VMI disappears for diffuse rescattering in Fig. 3(j). The significantly larger total yield η for diffuse rescattering, compared to specular rescattering, is consistent with PEs that are rescattered to smaller angles than the incident angle (relative to the surface normal at the turning point of the scattered trajectory on the NP) being more likely to escape. Note that this effect is absent if residual-charge interactions are neglected [cf. Figs. 3(e) and 3(i)], consistent with \vec{F}_{res} promoting rescattering.

4. Photoelectron correlation

In the third column of Fig. 3, we investigate the effects of PE correlation on VMIs. This column shows the results obtained by solving Newton’s equations (22) for the motion of released electrons under the influence of the electric fields of the incident laser \vec{E}_{inc} (1), induced plasmonic dipole \vec{E}_{pl} (3), and PE repulsion \vec{F}_{e-e} (23). In this column, the electric field of the residual charges \vec{F}_{res} (18) is neglected.

The addition of \vec{F}_{e-e} introduces Coulomb energy into the system of released electrons, accelerating a large fraction of PEs to significantly higher final (detectable) kinetic energies. Correspondingly, \vec{F}_{e-e} decreases the number of rescattering and recombination events (compare column 3 with columns

1 and 2 of Fig. 3). This results in distinctly larger PE cutoff energies compared to VMIs calculated without including PE correlation in columns 1 and 2 of Fig. 3. The larger cutoff energy is solely related to strong PE correlation and not to rescattering, since adding \vec{F}_{e-e} almost eliminates the effect of PE rescattering. This is seen in the lack of contrast between the VMIs and PE detection yields η in column 3. In opposition to the results excluding \vec{F}_{e-e} in columns 1 and 2, disallowing rescattering in Fig. 3(c) reduces the integrated yield η by only 9% and 10%, compared to specular and diffuse rescattering in Figs. 3(g) and 3(k), respectively. Thus, in comparison with the VMIs in column 2, the inclusion of PE correlation in column 3 strongly enhances direct emission (to 91% and 90%, respectively) to the detriment of PE rescattering. The slightly larger yield for diffuse rescattering, compared to specular rescattering, is consistent with smaller scattering angles (relative to the local surface normal), making PE recombination less likely. The large increase of the PE cutoff energy in Fig. 3(c) in comparison with Fig. 3(a) indicates that PE Coulomb repulsion dominates PE interactions with the incident laser and induced plasmonic fields in shaping the VMIs.

Apart from the increased cutoff energy, the Coulomb repulsion between PEs changes the shape of the elongated and dipolelike PEMDs shown without including \vec{F}_{e-e} in columns 1 and 2 of Fig. 3. \vec{F}_{e-e} renders the highest-energy part of the PE spectrum approximately isotropic, regardless of rescattering and recombination events, and leads to dominantly transverse PE emission. The enhanced transverse PE emission is visible as a horizontal structure confined by transverse PE velocities $|v_x| < 2$ a.u. and longitudinal velocities $|v_z|$ below approximately 0.5 a.u. We interpret this structure as due to the absence of the attractive residual-charge interactions and dominant direct emission in the simulated VMIs shown in the third column of Fig. 3. This horizontal structure is consistent with the rapid release of electrons near the poles of the NP (along the laser polarization direction), where strong-field tunneling ionization most likely occurs. During each laser half cycle this forms an initially spatially compact ensemble of electrons in the x - y plane near a NP pole with a narrow extension along the laser polarization direction (z axis) that is spread laterally by dominant PE-PE Coulomb repulsion.

5. Effect of all interactions

Simulated VMIs and relative PE yields η including all PE interactions, i.e., \vec{E}_{inc} (1), \vec{E}_{pl} (3), \vec{F}_{e-e} (23), and \vec{F}_{res} (18), are shown in the fourth column of Fig. 3. As expected, and easily seen in comparison with the VMIs in the third column, inclusion of the attractive residual-charge interactions decreases the PE cutoff energy and weakens the transverse emission at lower PE energies. The comparison of the VMIs in columns 1 and 4 of Fig. 3 reveals that the combined effect of \vec{F}_{e-e} and \vec{F}_{res} considerably increases the final energy of directly emitted electrons while decreasing the direct-emission yield from about 94% to less than 62%. Directly emitted PEs are slower than rescattered PEs. As a result, on average, directly emitted PEs move closer to the NP. They are thus (i) more likely to recombine with the NP, reducing the direct PE yield in the fourth column of Fig. 3, and (ii) experience a stronger Coulomb repulsion, leading to higher acceleration

and large final kinetic energies. Due to strong PE correlation, direct photoemission from metal NPs can reach cutoff energies exceeding $100U_p(I_0)$, which is about 75% the cutoff energy of rescattered PEs [cf. Figs. 3(d) and 3(l)].

To summarize the influence of different PE interactions, we first note that the linearly polarized incident laser and induced plasmonic electric field imprint their dipole character on the PEMDs in the absence of PE correlation and diffuse rescattering. The inclusion of PE correlation and diffuse rescattering removes the dipolar character of the VMIs and results in more isotropic PEMDs. For metal NPs, attractive residual-charge interactions are thus much less influential than PE correlation in shaping PEMDs and determining PE cutoff energies. In addition, we note that PE correlation significantly contributes to the high-energy part of the PE spectra, even for direct emission, resulting in cutoff energies way above the conventional $2U_p(I_0)$ limit of atomic targets [3] and even the $2\eta_{\text{pl}}^2 U_p(I_0)$ cutoff energy of dielectric NPs [24]. The increase of the PE cutoff energies due to rescattering (and compared to direct emission) is less pronounced for metal NPs than for gaseous atomic targets and dielectric NPs.

B. Photoemission dynamics

The VMIs in Fig. 3 are the end results of the intertwined evolution of electron emission, recombination, and competing electronic and laser-electron interactions. To examine the dynamics of these interactions, we show in Fig. 4 the incremental change per laser half cycle j of the numbers of emitted (n_{emi}) and recombined (n_{rec}) PEs as a function of time [cf. Eq. (10) and subsequent text]. These numbers are extracted in half-laser-cycle intervals during the laser-NP interaction from simulations for the same combinations of PE interactions distinguished in the four columns of Fig. 3. Electron numbers shown in Figs. 4(a) and 5(a) are calculated without allowing for PE rescattering [corresponding to the VMIs in Figs. 3(a)–3(d)] and including diffuse rescattering [corresponding to Figs. 3(i)–3(l)]. The corresponding electron-number evolutions for simulations including specular rescattering are in close agreement with the results in Figs. 4(b) and 5(b) and not displayed. According to Eq. (10), the incremental changes of these PE numbers during a given half cycle j are

$$\Delta n_{\text{emi},j}^{\kappa} = n_{\text{emi}}^{\kappa}(t_{\text{cyc},j}, t_{\text{cyc},j-1}), \quad (29)$$

$$\Delta n_{\text{rec},j}^{\kappa} = n_{\text{rec}}^{\kappa}(t_{\text{cyc},j}, t_{\text{cyc},j-1}), \quad \kappa = \text{pl, res, } e-e. \quad (30)$$

The superscripts refer to calculations in which only PE interactions with the laser and induced plasmonic electric field are included ($\kappa = \text{pl}$, corresponding to the VMIs in the first column in Fig. 3) and to simulations that add either PE-residual-charge interactions ($\kappa = \text{res}$, corresponding to the second column in Fig. 3) or PE Coulomb repulsion ($\kappa = e-e$, corresponding to the third column Fig. 3). Full simulations including all PE interactions are given the superscript $\kappa = \text{all}$ and correspond to the fourth column of Fig. 3. All electron numbers are shown as colored markers that are connected by solid and dotted lines to guide the eye. The numbers of propagated PEs for the same set of simulations as in Fig. 4 are shown in Fig. 5.

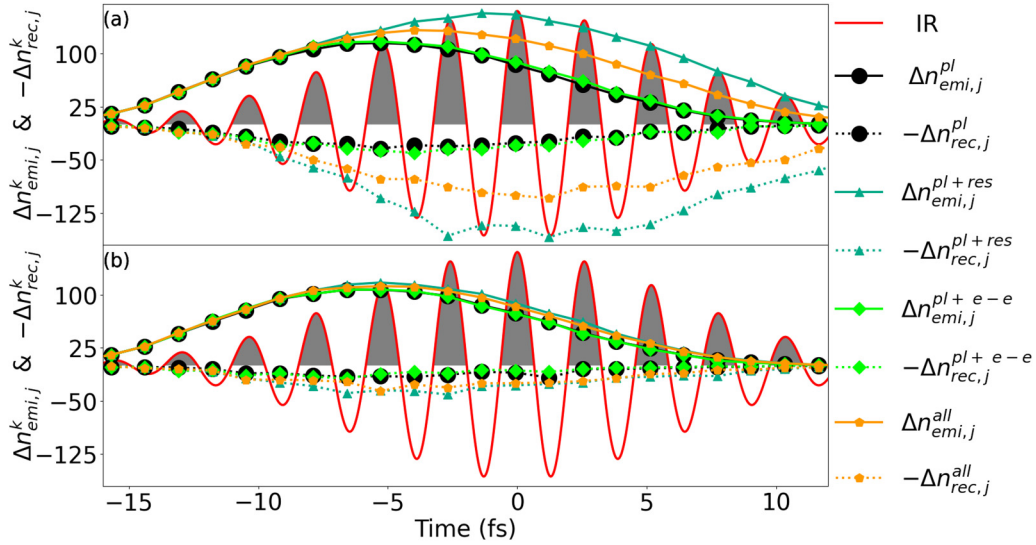


FIG. 4. Calculated numbers of emitted ($\Delta n_{emi,j}^{\kappa}$) and recombined ($\Delta n_{rec,j}^{\kappa}$) electrons in each laser half cycle j during the laser-NP interaction for 30-nm-diameter gold nanospheres, corresponding to the VMIs in (a) Figs. 3(a)–3(d) for no scattering and (b) Figs. 3(i)–3(l) for diffuse scattering. Subscripts refer to emitted and recombined electrons. Superscripts distinguish simulations including only the laser and induced plasmonic electric fields [$\kappa = pl$], corresponding to the VMI in Figs. 3(a) and 3(i) and simulations adding either PE–residual-charge interactions [$\kappa = res$; cf. Figs. 3(b) and 3(j)] or PE Coulomb repulsion [$\kappa = e-e$; cf. Figs. 3(c) and 3(k)]. Numbers of recombined PEs are multiplied by -1 for clarity. The calculated electron numbers are shown as colored markers that are connected by straight lines to guide the eye. The laser electric field is shown as the red solid line. The laser-pulse length, wavelength, and peak intensity are $\tau = 25$ fs, $\lambda = 780$ nm, and $I_0 = 8.0 \times 10^{12}$ W/cm², respectively.

The PE dynamics is governed by alternating (\vec{E}_{inc} and \vec{E}_{pl}), attractive (\vec{F}_{res}), and repulsive (\vec{F}_{e-e}) electric fields. The influence of the oscillating and repulsive forces on $n_{emi}(t)$, $n_{rec}(t)$, and $n_{pro}(t)$ is small, while the attractive interaction \vec{F}_{res} has a significant impact on them. Residual-charge interactions \vec{F}_{res} tend to increase the number of recombined PEs $n_{rec}(t)$. This increases the net electric field F on the surface by reducing the residual charge and thus increases $n_{emi}(t)$. As expected, this

is most clearly displayed in simulations in which otherwise rescattered PEs are assumed to recombine, shown in Figs. 4(a) and 5(a).

After the laser pulse has passed the NP (i.e., after approximately $\tau = 25$ fs), strong attractive residual-charge interactions prevent a fraction of low-energy PEs from escaping the NP. These trapped electrons typically either repeatedly rescatter or orbit the NP. They do not contribute to the detected

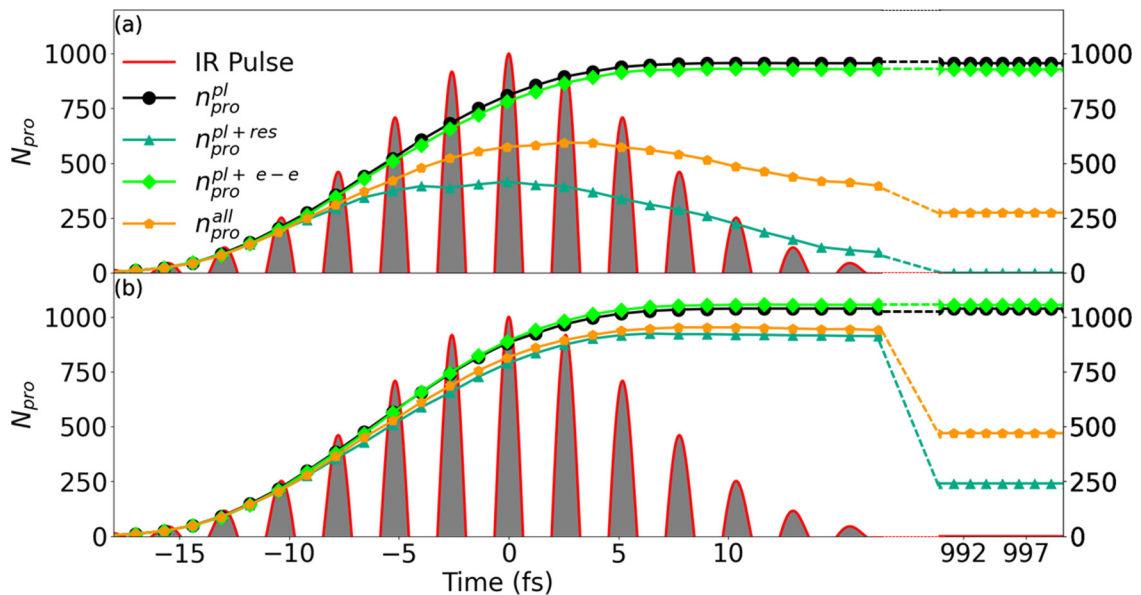


FIG. 5. Same as Fig. 4 for the time evolution of the accumulated number of propagated electrons $n_{pro}(t) = n_{emi}(-20 \text{ fs}, t) - n_{rec}(-20 \text{ fs}, t)$ for (a) no scattering and (b) diffuse scattering. Final converged electron numbers are shown on the right side.

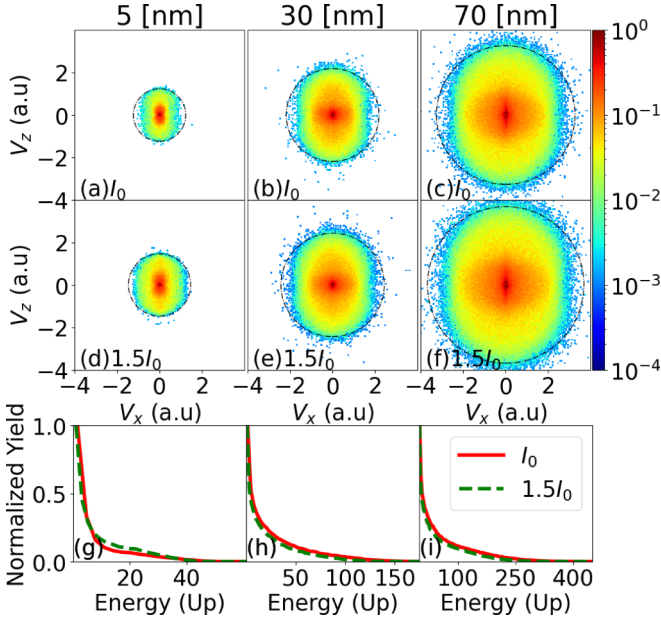


FIG. 6. Comparison of (a)–(f) VMIs and (g)–(i) integrated PE yields as functions of the PE kinetic energy, scaled by the incident-laser ponderomotive energy U_p , for gold nanospheres with 5-, 30-, and 70-nm-diameter and laser peak intensities of (a)–(c) $I_0 = 8.0 \times 10^{12}$ W/cm² and (d)–(f) $1.5I_0$. The laser-pulse length and wavelength are 25 fs and 780 nm, respectively. Black dashed circles in (a)–(f) indicate PE cutoff energies calculated from Eq. (32).

electron yield. Electrons on “trapped” trajectories screen the positive residual charges and are assumed to recombine. This assumption does not noticeably change the PE motion at large distances, where the PE interaction is dominated by the monopole term of the NP charge distribution. Due to the long-range residual-charge interactions, we carefully monitor the convergence of the trajectory calculations and propagate all PE trajectories for a sufficiently long time, to guarantee converged PEMDs. The right side of Fig. 5 shows the numbers of propagated PEs $n_{\text{pro}}(t)$ that have converged to the numbers of detected electrons after a propagation time of 1 ps.

C. Influence of nanoparticle size and laser intensity

Figure 6 shows PE VMIs and their integrated yields as a function of the PE kinetic energy for gold nanospheres with diameters of 5, 30, and 70 nm. Figures 6(a)–6(c) and 6(d)–6(f) compare corresponding simulated VMIs for laser peak intensities of $I_0 = 8.0 \times 10^{12}$ W/cm² and $1.5I_0$, respectively. Their corresponding integrated yields in Figs. 6(g)–6(i) are individually normalized to their maxima. The PEMDs in Figs. 6(a)–6(f) are slightly elongated along the laser-polarization direction, with PE cutoff energies that increase with NP size. As discussed in Sec. III A above, isotropic PEMDs are promoted by PE correlation and diffuse PE rescattering from the surface, while incident laser and induced plasmonic-field interactions tend to imprint a dipolar shape. The simulated VMIs also reveal the expected increase of the PE cutoff energy with the laser peak intensity. We quantify this laser intensity and NP-size-dependent effect in the following section.

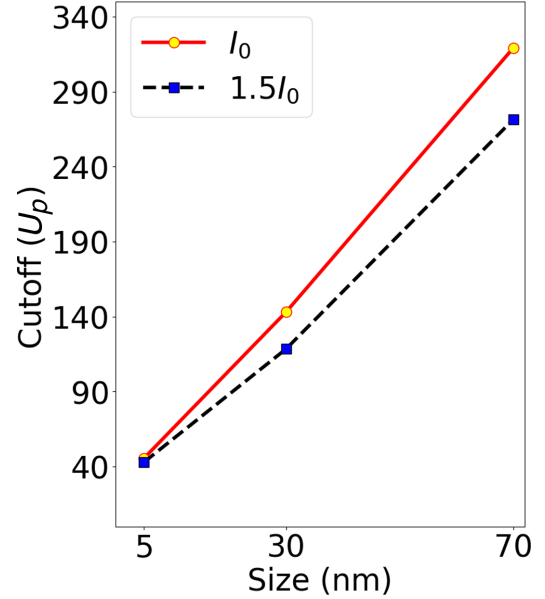


FIG. 7. Comparison of simulated PE cutoff energies, scaled by the incident-laser ponderomotive energy U_p , for 5-, 30-, and 70-nm-diameter gold nanospheres and laser peak intensities of $I_0 = 8.0 \times 10^{12}$ W/cm² and $1.5I_0$. The laser-pulse length and wavelength are the same as in Fig. 6.

D. Angle-integrated photoelectron yields and cutoff energies

Integration of the VMI-projected PEMDs $y(v_x, v_z)$ in Figs. 6(a)–6(f) over the PE detection angles ϕ in the VMI plane results in the PE yields

$$Y(E_{\text{PE}}) = \int d\phi y(\sqrt{2E_{\text{PE}}} \cos \phi, \sqrt{2E_{\text{PE}}} \cos \phi) \quad (31)$$

as a function of the PE energy in the VMI plane, $E_{\text{PE}} = (v_x^2 + v_z^2)/2$. The yields $Y(E_{\text{PE}})$ shown in Figs. 6(g)–6(i) are normalized individually to their maxima.

We define the PE cutoff energy E_{cutoff} by integrating over the yield given by Eq. (31) as the PE energy up to which 99% of the total PE yield have accumulated,

$$\frac{\int_0^{E_{\text{cutoff}}} dE_{\text{PE}} Y(E_{\text{PE}})}{\int_0^{\infty} dE_{\text{PE}} Y(E_{\text{PE}})} = 99\%. \quad (32)$$

Photoelectron cutoff energies are shown as black dashed circles in Figs. 6(a)–6(f) and as circular and square markers in Fig. 7. They increase with the NP size and slightly decrease with the selected peak laser intensities. The red solid lines with yellow circles and black dashed lines with blue squares in Fig. 7 denote cutoff energies for peak laser intensities of $I_0 = 8.0 \times 10^{12}$ W/cm² and $1.5I_0$, respectively, in units of the incident laser ponderomotive energies $U_p(I_0)$ and $U_p(1.5I_0)$. The intensity-dependent change of E_{cutoff} becomes more pronounced for larger NP diameters.

Based on the discussion of the different PE interactions and their influence on PEMDs in the preceding sections, we investigate two plausible causes for the numerically predicted increase of the PE yield and cutoff energy with the NP size. First, as the NP size increases, a larger surface area becomes available from where more electrons are emitted, increasing

the PE yield. We directly attribute the increase in yield to this effect and relate the increase of the cutoff energy indirectly to the NP size, as the increased PE yield entails more Coulomb energy between PEs upon their release from the NP surface. In addition, we note that even though for larger NPs multiple rescattering is more likely to occur, our numerical tests, allowing for no more than one rescattering events per PE, showed no visible change in the simulated VMIs and corresponding cutoff energies. We thus attribute single rescattering to the numerically predicted cutoff-energy increase with size, allowing the PE to gain a significant amount of kinetic energy from the incident laser pulse.

The second cause for our numerically observed increase of the PE yield and cutoff energy with the NP size is the lowering and narrowing of the surface-potential barrier, due to the more significant nanoplasmonic field enhancement near larger NPs [38,43,44,57] promoting strong-field tunneling ionization. This not only tends to augment the measured PE yield, but since PEs gain more energy in a more strongly enhanced field, it also entails higher cutoff energies for larger NP sizes.

As discussed in Sec. III A, the effects of residual-charge interactions and PE correlation oppose each other. While attractive residual-charge–PE interactions reduce both PE yield and cutoff energy, PE Coulomb repulsion increases them. Our numerical results indicate that PE Coulomb repulsion dominates over residual-charge–PE interactions with regard to the cutoff energy, resulting in a net cutoff-energy increase. With regard to the PE yield, the situation is reversed. Here the residual-charge–PE interaction dominates over PE correlation. Since the number of emitted PE increases with the NP size, we find larger cutoff energies for larger NPs.

For gaseous atomic targets [2–5] and dielectric NPs [24], the cutoff energy is proportional to the ponderomotive energy U_p . In contrast, our results for metal NPs in Fig. 7 start to increasingly deviate from the linear scaling in U_p as the NP size increases. Although at the higher intensity $1.5I_0$ the induced plasmonic field and PE Coulomb repulsion are stronger, our numerically calculated VMIs indicate that the increasing accumulation of residual charges on the NP becomes the determining factor. This reduces the scaled cutoff energy at the larger considered intensity. This reduction is more pronounced for larger NPs, due to stronger plasmonic field enhancement.

We note that our modeling does not include electron-impact ionization. While we expect electron-impact ionization to increase the yield in the low-energy part of the PE spectrum, it is not likely to change the PE cutoff energy, simply because the energy initially transferred in the plasmonically enhanced incident field to one electron is shared by two (or more) electrons. This expectation is confirmed by the favorable comparison of our calculated with unpublished measured

cutoff energies [63]. We expect the effect of electron-impact ionization on the PE yield to be rather limited, due to the simultaneous addition of positive residual charges. A detailed comparison of our model calculations with recently measured data is in progress, but is beyond the scope of the present paper.

IV. CONCLUSION

We modeled strong-field ionization from metal NPs and numerically simulated PEMDs as experimentally accessible by VMI spectrometry. Our simulations scrutinize a complex dynamical interplay of PE emission, propagation, recombination, and rescattering. Augmented by strong plasmonic field enhancement, a large number of PEs tunnel ionize from metal NPs and result in high PE yields and cutoff energies. We analyzed the size and laser-intensity dependence of PE angular distributions in light of competing contributions from various PE interactions.

In particular, we found that the dipolar shape, imprinted on PEMDs by the incident laser and induced plasmonic fields, is mostly erased by PE correlations and diffusive PE rescattering at the NP surface to yield almost isotropical VMIs. While for gaseous atomic targets, nanotips [18–23], and dielectric NPs [24–26] directly emitted PEs acquire no more than about 20% of the cutoff energy for rescattered PEs [$10U_p(I_0)$ atomic targets and $10\eta_{pl}^2 U_p(I_0)$ for nanotip and dielectric NPs], we have shown that direct photoemission from 30-nm metal NPs results in cutoff energies of $100U_p(I_0)$ and further increases for larger NPs, reaching about 75% of the cutoff energy for rescattered PEs. In addition, due to laser-intensity-dependent PE emission, the effects of residual charges and electron-electron interactions are highly intensity dependent. This leads to a nonlinear intensity dependence of the PE yield and cutoff energy scaling with $U_p(I_0)$, contrary to the known linear intensity scaling for gaseous atomic targets.

ACKNOWLEDGMENTS

We thank Reza Mazloom, Jeffrey Powell, Artem Rudenko, Adam Summers, and Aram Vajdi for stimulating discussions. E.S. and J.L. were supported in part by the Air Force Office of Scientific Research Award No. FA9550-17-1-0369 (Recollision Physics at the Nanoscale). E.S. and U.T. were supported in part by NSF Grant No. PHY 2110633 (Transient Strong-Field Dielectric Response of Nanoparticles). U.T. acknowledges partial support from the Chemical Sciences, Geosciences, and Biosciences Division, Office of Basic Energy Sciences, Office of Science, U.S. DOE under Award No. DE-FG02-86ER13491 (Attosecond Interferometry and Photoemission from Atoms in Spatially Varying External Fields).

-
- [1] L. Keldysh, *Sov. Phys. JETP* **20**, 1307 (1965).
 [2] G. G. Paulus, W. Becker, W. Nicklich, and H. Walther, *J. Phys. B* **27**, L703 (1994).
 [3] B. Walker, B. Sheehy, K. C. Kulander, and L. F. DiMauro, *Phys. Rev. Lett.* **77**, 5031 (1996).
 [4] W. Becker, F. Grasbon, R. Kopold, D. B. Milošević, G. G.

Paulus, and H. Walther, *Adv. At. Mol. Opt. Phys.* **48**, 35 (2002).

- [5] W. Becker, S. P. Goreslavski, D. B. Milošević, and G. G. Paulus, *J. Phys. B* **51**, 162002 (2018).
 [6] S. Ghimire, A. D. DiChiara, E. Sistrunk, P. Agostini, L. F. DiMauro, and D. A. Reis, *Nat. Phys.* **7**, 138 (2011).

- [7] M. J. Ambrosio and U. Thumm, *Phys. Rev. A* **97**, 043431 (2018).
- [8] M. J. Ambrosio and U. Thumm, *Phys. Rev. A* **100**, 043412 (2019).
- [9] F. Navarrete and U. Thumm, *Phys. Rev. A* **102**, 063123 (2020).
- [10] V. E. Nefedova, S. Fröhlich, F. Navarrete, N. Tancogne-Dejean, D. Franz, A. Hamdou, S. Kaassamani, D. Gauthier, R. Nicolas, G. Jargot *et al.*, *Appl. Phys. Lett.* **118**, 201103 (2021).
- [11] L. Xue, S. Liu, Y. Hang, A. M. Summers, D. J. Wilson, X. Wang, P. Chen, T. G. Folland, J. A. Hachtel, H. Shi *et al.*, [arXiv:2101.10429](https://arxiv.org/abs/2101.10429).
- [12] F. Navarrete, M. F. Ciappina, and U. Thumm, *Phys. Rev. A* **100**, 033405 (2019).
- [13] T. Ditmire, J. Zweiback, V. Yanovsky, T. Cowan, G. Hays, and K. Wharton, *Nature (London)* **398**, 489 (1999).
- [14] J. Passig, R. Irsig, N. X. Truong, T. Fennel, J. Tiggesbäumker, and K. H. Meiwes-Broer, *New J. Phys.* **14**, 085020 (2012).
- [15] C. Varin, C. Peltz, T. Brabec, and T. Fennel, *Ann. Phys. (Berlin)* **526**, 135 (2014).
- [16] T. Lünskens, P. Heister, M. Thämer, C. A. Walenta, A. Kartouzian, and U. Heiz, *Phys. Chem. Chem. Phys.* **17**, 17541 (2015).
- [17] Z. Wang, A. Camacho Garibay, H. Park, U. Saalman, P. Agostini, J. M. Rost, and L. F. DiMauro, *Phys. Rev. Lett.* **124**, 173201 (2020).
- [18] G. Herink, D. R. Solli, M. Gulde, and C. Ropers, *Nature (London)* **483**, 190 (2012).
- [19] M. Müller, V. Kravtsov, A. Paarmann, M. B. Raschke, and R. Ernstorfer, *ACS Photon.* **3**, 611 (2016).
- [20] M. Krüger, M. Schenk, and P. Hommelhoff, *Nature (London)* **475**, 78 (2011).
- [21] G. Wachter, Ph.D. thesis, Vienna University of Technology, 2014.
- [22] M. Krüger, M. Schenk, P. Hommelhoff, G. Wachter, C. Lemell, and J. Burgdörfer, *New J. Phys.* **14**, 085019 (2012).
- [23] G. Wachter, C. Lemell, J. Burgdörfer, M. Schenk, M. Krüger, and P. Hommelhoff, *Phys. Rev. B* **86**, 035402 (2012).
- [24] S. Zherebtsov, T. Fennel, J. Plenge, E. Antonsson, I. Znakovskaya, A. Wirth, O. Herrwerth, F. Süßmann, C. Peltz, I. Ahmad *et al.*, *Nat. Phys.* **7**, 656 (2011).
- [25] F. Süßmann and M. F. Kling, *Phys. Rev. B* **84**, 121406(R) (2011).
- [26] L. Seiffert, Q. Liu, S. Zherebtsov, A. Trabattani, P. Rupp, M. Castrovillani, M. Galli, F. Süßmann, K. Wintersperger, J. Stierle *et al.*, *Nat. Phys.* **13**, 766 (2017).
- [27] P. B. Corkum, *Phys. Rev. Lett.* **71**, 1994 (1993).
- [28] G. Mie, *Ann. Phys. (Leipzig)* **330**, 377 (1908).
- [29] J. A. Stratton, *Electromagnetic Theory* (Wiley, New York, 2007).
- [30] F. Süßmann, L. Seiffert, S. Zherebtsov, V. Mondes, J. Stierle, M. Arbeiter, J. Plenge, P. Rupp, C. Peltz, A. Kessel *et al.*, *Nat. Commun.* **6**, 7944 (2015).
- [31] Q. Liu, L. Seiffert, F. Süßmann, S. Zherebtsov, J. Passig, A. Kessel, S. A. Trushin, N. G. Kling, I. Ben-Itzhak, V. Mondes *et al.*, *ACS Photon.* **7**, 3207 (2020).
- [32] M. V. Ammosov, *Sov. Phys. JETP* **64**, 1191 (1987).
- [33] J. A. Powell, A. M. Summers, Q. Liu, S. J. Robotjazi, P. Rupp, J. Stierle, C. Trallero-Herrero, M. F. Kling, and A. Rudenko, *Opt. Express* **27**, 27124 (2019).
- [34] K. L. Kelly, E. Coronado, L. L. Zhao, and G. C. Schatz, *J. Phys. Chem. B* **107**, 668 (2003).
- [35] L. Wang, M. Hasanzadeh Kafshgari, and M. Meunier, *Adv. Funct. Mater.* **30**, 2005400 (2020).
- [36] J. A. Powell, J. Li, A. Summers, S. J. Robotjazi, M. Davino, P. Rupp, E. Saydanzad, C. M. Sorensen, D. Rolles, M. F. Kling *et al.*, [arXiv:2108.06872](https://arxiv.org/abs/2108.06872).
- [37] M. I. Stockman, *Phys. Today* **64**(2), 39 (2011).
- [38] J. Li, E. Saydanzad, and U. Thumm, *Phys. Rev. A* **95**, 043423 (2017).
- [39] S. Link and M. A. El-Sayed, *J. Phys. Chem. B* **103**, 4212 (1999).
- [40] P. K. Jain, X. Huang, I. H. El-Sayed, and M. A. El-Sayed, *Plasmonics* **2**, 107 (2007).
- [41] E. Le Ru and P. Etchegoin, *Principles of Surface-Enhanced Raman Spectroscopy and Related Plasmonic Effects* (Elsevier, Oxford, 2008).
- [42] M. I. Stockman, M. F. Kling, U. Kleineberg, and F. Krausz, *Nat. Photon.* **1**, 539 (2007).
- [43] E. Saydanzad, J. Li, and U. Thumm, *Phys. Rev. A* **95**, 053406 (2017).
- [44] J. Li, E. Saydanzad, and U. Thumm, *Phys. Rev. A* **94**, 051401(R) (2016).
- [45] A. Kabashin, P. Evans, S. Pastkovsky, W. Hendren, G. Wurtz, R. Atkinson, R. Pollard, V. Podolskiy, and A. Zayats, *Nat. Mater.* **8**, 867 (2009).
- [46] K. A. Willets and R. P. Van Duyne, *Annu. Rev. Phys. Chem.* **58**, 267 (2007).
- [47] L. Wang, C. Darvot, J. Zapata-Farfan, S. Patskovsky, D. Trudel, and M. Meunier, *J. Biophoton.* **12**, e201900166 (2019).
- [48] A. M. Wilson, J. Mazzaferri, E. Bergeron, S. Patskovsky, P. Marcoux-Valiquette, S. Costantino, P. Sapieha, and M. Meunier, *Nano. Lett.* **18**, 6981 (2018).
- [49] T. Chen and B. M. Reinhard, *Adv. Mater.* **28**, 3522 (2016).
- [50] A. E. Schlather, A. Manjavacas, A. Lauchner, V. S. Marangoni, C. J. DeSantis, P. Nordlander, and N. J. Halas, *J. Phys. Chem. Lett.* **8**, 2060 (2017).
- [51] M. T. Sheldon, J. Van de Groep, A. M. Brown, A. Polman, and H. A. Atwater, *Science* **346**, 828 (2014).
- [52] S. Liu, R. Jiang, P. You, X. Zhu, J. Wang, and F. Yan, *Energy Environ. Sci.* **9**, 898 (2016).
- [53] A. M. Gobin, M. H. Lee, N. J. Halas, W. D. James, R. A. Drezek, and J. L. West, *Nano Lett.* **7**, 1929 (2007).
- [54] C. Ayala-Orozco, C. Urban, M. W. Knight, A. S. Urban, O. Neumann, S. W. Bishnoi, S. Mukherjee, A. M. Goodman, H. Charron, T. Mitchell *et al.*, *ACS Nano* **8**, 6372 (2014).
- [55] F. Krausz and M. I. Stockman, *Nat. Photon.* **8**, 205 (2014).
- [56] G. Baffou and R. Quidant, *Laser Photon. Rev.* **7**, 171 (2013).
- [57] E. Saydanzad, J. Li, and U. Thumm, *Phys. Rev. A* **98**, 063422 (2018).
- [58] J. Li, E. Saydanzad, and U. Thumm, *Phys. Rev. Lett.* **120**, 223903 (2018).
- [59] R. H. Fowler and L. Nordheim, *Proc. R. Soc. London Ser. A* **119**, 173 (1928).
- [60] J. H. B. Deane and R. G. Forbes, *J. Phys. A: Math. Theor.* **41**, 395301 (2008).
- [61] S. Anisimov, B. Kapeliovich, and T. Perelman, *Zh. Eksp. Teor. Fiz.* **66**, 776 (1974).
- [62] J. L. Ellis, D. D. Hickstein, W. Xiong, F. Dollar, B. B. Palm, K. E. Keister, K. M. Dorney, C. Ding, T. Fan, M. B. Wilker *et al.*, *J. Phys. Chem. Lett.* **7**, 609 (2016).

- [63] J. A. Powell, Ph.D. thesis, Kansas State University, 2017.
- [64] C. S. Kumarasinghe, M. Premaratne, Q. Bao, and G. P. Agrawal, *Sci. Rep.* **5**, 12140 (2015).
- [65] P. Narang, R. Sundararaman, and H. A. Atwater, *Nanophotonics* **5**, 96 (2016).
- [66] J. D. Jackson, *Classical Electrodynamics*, 3rd ed. (Wiley, New York, 1999).
- [67] H. Kuwata, H. Tamaru, K. Esumi, and K. Miyano, *Appl. Phys. Lett.* **83**, 4625 (2003).
- [68] S. A. Maier, *Plasmonics: Fundamentals and Applications* (Springer, New York, 2007).
- [69] P. B. Johnson and R.-W. Christy, *Phys. Rev. B* **6**, 4370 (1972).
- [70] M. N. Sadiku, *Elements of Electromagnetics* (Oxford University Press, New York, 2018).
- [71] N. Ashcroft and N. Mermin, *Solid State Physics* (Saunders, Philadelphia, 1976).
- [72] E. L. Murphy and R. Good, Jr., *Phys. Rev.* **102**, 1464 (1956).
- [73] R. G. Forbes, *Appl. Phys. Lett.* **89**, 113122 (2006).
- [74] S. C. Singh, H. Zeng, C. Guo, and W. Cai, *Nanomaterials: Processing and Characterization with Lasers* (Wiley, New York, 2012).
- [75] L. L. Dasallas and W. O. Garcia, *Mater. Res. Express* **5**, 016518 (2018).
- [76] C. F. Bohren and D. R. Huffman, *Absorption and Scattering of Light by Small Particles* (Wiley, New York, 2008).
- [77] C. Voisin, N. Del Fatti, D. Christofilos, and F. Vallée, *J. Phys. Chem. B* **105**, 2264 (2001).
- [78] R. G. Forbes, *J. Vac. Sci. Technol. B* **26**, 788 (2008).
- [79] M. H. Kalos and P. A. Whitlock, *Monte Carlo Methods* (Wiley, Weinheim, 2008).
- [80] W. M. Haynes, *CRC Handbook of Chemistry and Physics* (CRC, Boca Raton, 2014).